Photocatalytic Hydrogen Production of Nd/Co Co-Doped BiFeO₃ Nanoparticles With a Cellular Architecture

Yanhong Gu[1]*, Yan Zhou[2], Yanliang Yang[3], Xianghui Zhang[1], Weiying Zhang[1], Jianguo Zhao[1] and Hong Jia[1]*

[1]Key Lab Electromagnet Transformat and Detect Henan, School of Physics and Electronic Information, Luoyang Normal College, Luoyang, China, [2]School of Physics and Electronics, Institute of Microsystem, Henan University, Kaifeng, China, [3]Henan Key Laboratory of Function-Oriented Porous Material, College of Chemistry and Chemical Engineering, Luoyang Normal University, Luoyang, China

Bismuth ferrite (BFO) nanoparticle with general formula $Bi_{1-x}Nd_xFe_{1-y}Co_yO_3$ (x=0, 0.05; y=0, 0.05, 0.10, 0.15, 0.20) were prepared using a two-solvent sol-gel method. Interestingly, most of the samples exhibited a cellular architecture. Bandgap engineering of BFO nanoparticles was achieved by co-doping with Nd and Co. Under illumination with ultraviolet light, the concentration of methylene orange increased. The sample of $Bi_{0.95}Nd_{0.05}Fe_{0.85}Co_{0.15}O_3$ produced a small amount of hydrogen ($8.88 molg^{-1}$ after 1.5;h), but the other samples did not produce detectable levels of hydrogen. In this research, the production of hydrogen occurred under illumination by ultraviolet light, demonstrating the splitting of pure water without the use of a sacrificial reagent. A possible reason for this is that the conduction and valence band edges of $BiFeO_3$ straddle the water redox potential. Consequently, it is possible to realize unassisted water splitting using BFO. The ferromagnetism of all samples increased linearly with the increase of dopant concentration, and the residual magnetization of the $Bi_{0.95}Nd_{0.05}Fe_{0.80}Co_{0.20}O_3$ sample reached to 0.679 emu g^{-1}. Moreover, the magnetic properties of bismuth ferrite and Nd/Co Co-doped bismuth ferrite photocatalyst were also investigated to show the simple separation. These results demonstrate that BFO nanoparticles have potential applications in photocatalytic hydrogen production without the use of a sacrificial reagent.

Keywords: BiFeO₃ nanoparticles, band gap, production of hydrogen, magnetic properties, cellular architecture

INTRODUCTION

Multiferroics have attracted the attention of researchers worldwide in recent years is because they exhibit a magnetoelectric coupling effect and have broad application prospects in information storage, electronic devices, and sensors. Bismuth ferrite ($BiFeO_3$, or BFO) stands out among multiferroics because of its magnetic and strong ferroelectric properties at room temperature (Dutta et al. 2010). The ferroelectricity of BFO is related to the Bi 6s lone electron pair at the A site, and the magnetic properties are related to the space-modulated spin structure. However, the cycloidal spin structure with a period of 62 nm leads to BFO having weak magnetic properties

(Puhan et al. 2019). When other elements are substituted for the A and B positions in BFO nanoparticles, there is a significant effect on the lattice structure and the Bi 6s lone pair, thus affecting ferroelectricity and ferromagnetism (Layek et al. 2013). It has been reported that the incorporation of Nd^{3+} at the A site of BFO can alter the ferromagnetism of the material (Yuan et al. 2006). Wang et al. noted that the incorporation of Nd^{3+}/Mn^{2+} at the A and B positions of BFO affects its structure and properties, and the incorporation of Nd^{3+} induces a phase transition from an R3c crystal structure to Pnma (Wang et al. 2019). Co-doping with Co and Eu successfully enhances the magnetic and dielectric properties of BFO nanoparticles. The significant enhancement of the saturation magnetization (M_s) upon co-doping with Eu and Co may be due to the destruction of the space-modulated spin structure (Das et al. 2012).

In addition, BFO has a narrow band gap (2.2 eV) and excellent chemical stability, and can be used as a photocatalyst to degrade organic pollutants and decompose water (Luo and Maggard, 2006; Li et al. 2010; Cheng et al. 2016). Bismuth Ferrite nanohybrids display improved photocatalytic activity and degradative ability (Fatima et al. 2020; Fatima et al., 2018; Iqbal et al. 2019a; Iqbal et al. 2019b). Compared with photoelectrochemical (PEC) water splitting, the photocatalytic dissociation of water has many advantages, such as being suited to splitting water of a nearly neutral pH in a one-step process without the need for an applied external bias. However, unassisted overall water splitting under a single-absorber photocatalytic process must achieve the following two conditions: 1) the valence and conduction gap edges of this photocatalyst must astride across the water oxidation (redox) and proton reduction and potentials; 2) this photocatalyst must possess a adequate narrow bandgap to absorb a majority of the solar spectrum (Fang and Shangguan, 2019). Due to such rigorous requirement, there are very few suitable photocatalyst. Moreover, efficient charge separation is a critical issue. Bismuth ferrite is one kind of special functional material that can be modified to exhibit the required space charge region, with an accumulation layer and a depletion layer, by using n-type and p-type doping. The band bending in this space charge region can be tuned to be favorable for the separation of excited electrons and holes. In addition, for applications in the photocatalyst field, one advantage of $BiFeO_3$ is its excellent magnetic properties. It is essential to separate photocatalyst after they have been synthesized. Generally, coagulation, flocculation, and sedimentation are widely used as separation processes, but they are complex and expensive (Fang and Shangguan, 2019; Reddy et al. 2019). The separation process is greatly simplified if the photocatalyst is magnetized, as this allows separation by the application of an external magnetic field (Yang et al., 2018).

Chowdhury et al. reported unassisted high-efficiency splitting of pure water using a $BiFeO_3$ diode (Chowdhury et al. 2018). Cheng et al. reported the production of hydrogen through the use of a ferroelectric polarization-mediated $Si/STO/BiFeO_3$ tandem photocathode (Cheng et al. 2016). In this work, however, we wanted to prepare a material

FIGURE 1 | Schematic diagram of hydrogen generation set-up working at negative pressure.
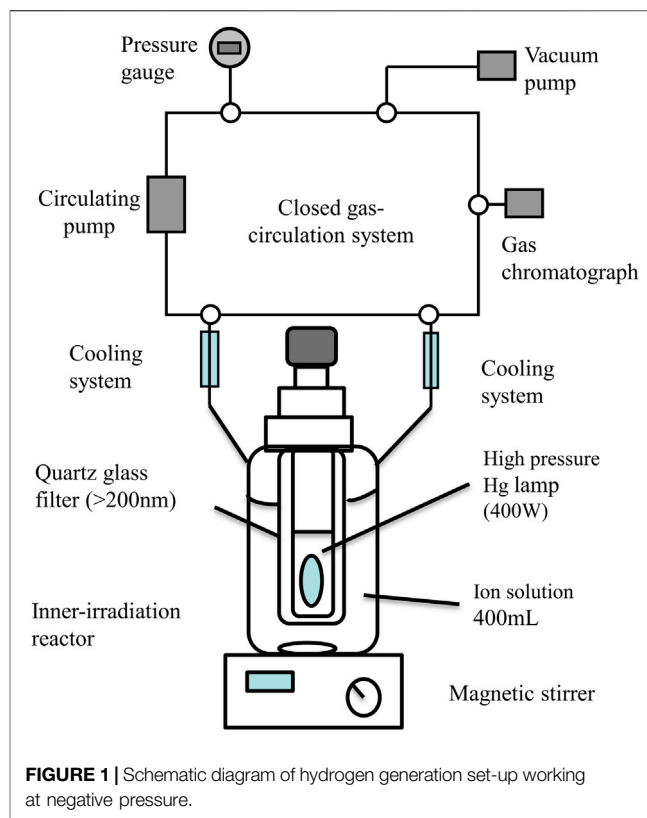
that could directly produce hydrogen through splitting water solely under illumination, without the use of a sacrificial agent or an external bias field. To achieve this, we simultaneously doped Nd^{3+} and Co^{2+} into the A and B sites of BFO, respectively. $Bi_{1-x}Nd_xFe_{1-y}Co_yO_3$ nanoparticles with different doping concentrations were synthesized using a sol-gel method. The effects of doping on the morphology, structure, magnetic properties, and bandgap of BFO nanoparticles were investigated.

Experiment

The $Bi_{1-x}Nd_xFe_{1-y}Co_yO_3$ (x = 0, 0.05; y = 0, 0.05, 0.10, 0.15, 0.20) as abbreviated BFO($BiFeO_3$), BNFO ($Bi_{0.95}Nd_{0.05}FeO_3$), BNFCO-5 ($Bi_{0.95}Nd_{0.05}Fe_{0.95}Co_{0.05}O_3$), BNFCO-10 ($Bi_{0.95}Nd_{0.05}Fe_{0.90}Co_{0.10}O_3$), BNFCO-15 ($Bi_{0.95}Nd_{0.05}Fe_{0.85}Co_{0.15}O_3$), BNFCO-20 ($Bi_{0.95}Nd_{0.05}Fe_{0.80}Co_{0.20}O_3$) nanoparticles were synthesized by two solvent sol-gel method, all reagents were of analytical grade. Bismuth nitrate pentahydrate (99.0% purity 0.01 mol) and neodymium nitrate hexahydrate (99.0% purity) are dissolved in a mixture of ethylene glycol (20 ml) and acetic acid (20 ml) in a certain proportion, stirred for 90 min at room-temperature. Since the Bi element is easily volatilized by heat, it is excessively 5%. Ferric nitrate (98.5% purity) and cobaltous nitrate (99.0% purity) are dissolved in a mixture of ethylene glycol (20 ml) and acetic acid (20 ml) in a certain proportion, stirred for 90 min at room-temperature. After this, both solutions were mixed and put under constant stirring for 3 h at room-temperature. Afterward, the precursor solution was dried at 80°C for 24 h and then grinded
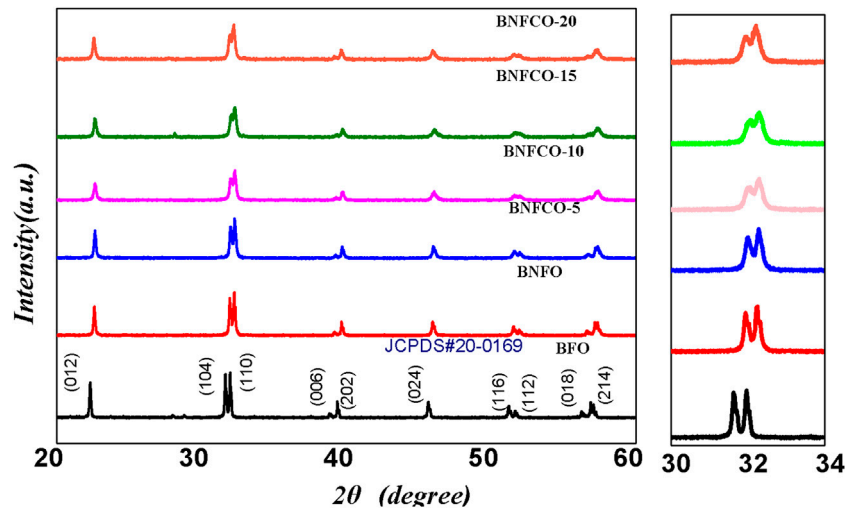
FIGURE 2 | XRD patterns of $Bi_{1-x}Nd_xFe_{1-y}Co_yO_3$ (x = 0, 0.05; y = 0, 0.05, 0.10, 0.15, 0.20) samples, with an enlarged view of the (104) and (110) diffraction peaks near the diffraction angle $2\theta = 32°$.

into powder. The powder was raised to 600°C at 2°C/min and calcined at 600° C for 3 h to form $Bi_{1-x}Nd_xFe_{1-y}Co_yO_3$ nanoparticles.

The phase constitutions and structure of the prepared samples were characterized by an X-ray diffraction (XRD) in the range of $2\theta = (20^0 – 60^0)$ and Raman scattering spectra. The morphology of the prepared samples was determined using scanning electron microscopy (SEM). The band-gap of the prepared samples was studied by UV-vis diffused reflectance spectra via UV-vis spectrophotometer. Room temperature magnetic properties of prepared samples were studied by vibrating sample magnetometer (VSM) in the −20 to 20 kOe field range.

The abilities of photocatalytic hydrogen production were conducted in an evacuation system (Beijing Perfect Light Technology Co., Ltd. China) and a Labsolar-III AG closed gas circulation, of which the system maintained the photo-reaction temperature at 5°C with a low-temperature thermostat bath (Poly Science, United States). The nanoparticles were irradiated by the simulated sunlight, which is A 300 W Xennon lamp (PLS-SXE-300UV, Beijing Trusttech Co. Ltd., China) with a UV-cutoff filter (providing visible light $\lambda \geq 420$ nm). a volume of 1.5 ml of gas was hourly sampled and measured by a gas chromatography equipped with a thermal conductivity detector (TCD) and a 5 Å molecular sieve column, so as to identify and quantify the production of gas. At the same time, inert gas argon (Ar) was applied as the carrier gas. The implementation details and schematic diagram of experimental process is shown in **Figure 1**.

RESULTS AND DISCUSSIONS

The X-ray diffraction (XRD) profiles of different samples are showed in **Figure 2**. From the result of the XRD patterns, all samples have perovskite structure and no other phases such as $Bi_2Fe_4O_9$ and $Bi_{25}FeO_{40}$ could be detected. The diffraction peaks of doped BFO nanoparticles had a tendency to shift toward higher
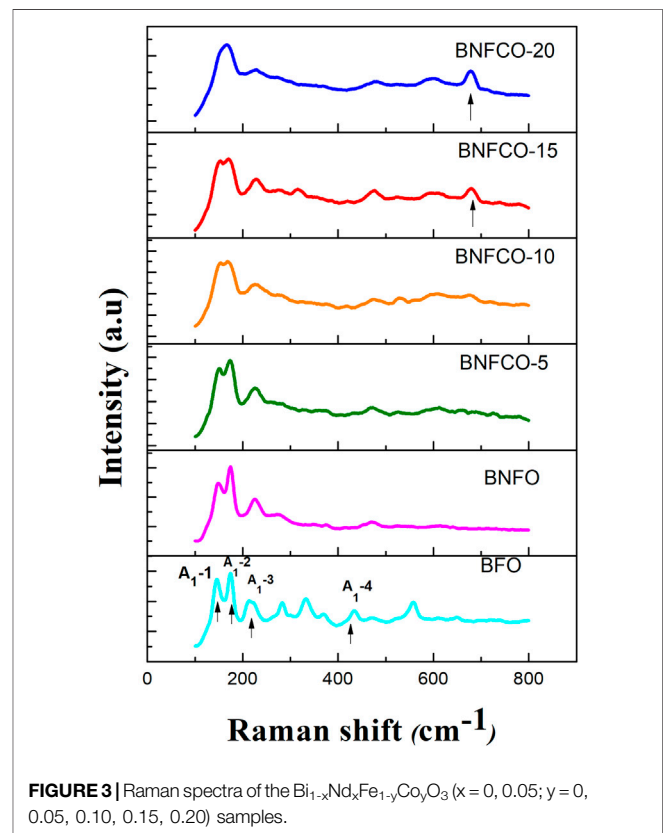
FIGURE 3 | Raman spectra of the $Bi_{1-x}Nd_xFe_{1-y}Co_yO_3$ (x = 0, 0.05; y = 0, 0.05, 0.10, 0.15, 0.20) samples.

diffraction angles when compared with the peaks of pure BFO. This is because the doped ionic radius is small and the unit cell volume is reduced, which shifts the diffraction peaks to higher diffraction angles. Similar phenomena are observed when other rare earth elements are incorporated (Lü et al. 2017) . As the doping ratio increases, the double diffraction peaks of the sample

TABLE 1 | Comparison of Raman mode frequency in the literature with this experiment (BFO).

Raman mode (cm^{-1})	This study	Yang et al. (2009)	Kothari et al. (2008)	Fukumura et al. (2007)	Singh et al. (2006)	Yuan et al. (2007)
A_1-1	146	139	135.15 ± 1.38	147	136	152.6
A_1-2	175.25	172	167.08 ± 0.34	176	168	177.5
A_1-3	213.25	217	218.11 ± 0.45	227	211	224.2
A_1-4	435.25	470	430.95 ± 16.69	490	425	—
E	283.25	275	255.38 ± 0	265	275	270
E	333.5	307	283.0 ± 0	279	335	298.8
E	370	345	351.55 ± 8.66	351	365	354.9
E	—	369	321.47 ± 3.76	375	—	—
E	472.2	429	467.6 ± 2.46	437	456	473.3
E	558.5	521	526.22 ± 2.27	473	549	554.3
E	611.25	613	598.84 ± 1.99	525	597	618.3
E	—	—	71.39 ± 0.11	77	—	—
E	—	—	98.36 ± 3.11	136	—	—

TABLE 2 | The $Bi_{1-x}Nd_xFe_{1-y}Co_yO_3$ nanoparticles Samples Raman mode frequency comparison.

Samples	Raman mode (cm^{-1})									
	A_1-1	A_1-2	A_1-3	A_1-4	E-2	E-3	E-4	E-5	E-6	E-7
BFO	146	175.25	213.25	435.25	283.25	333.5	370	472.5	558.5	611.25
BNFO	149	175	226	415.25	274.5	347.75	375.5	472.5	556.25	615.25
BNFCO-5	151.5	174.25	227.5	433.25	282	330.5	376.5	473.25	527.5	611
BNFCO-10	154	171	230	419	284	329.5	377	476.5	530.5	608
BNFCO-15	155.75	171	230	419	277.25	317.75	360	478.25	527	608
BNFCO-20	—	169.75	229.75	—	276.5	—	370.25	480.5	526.75	601.5

gradually merge into a single peak in the diffraction angle (2θ) range 31°33°. These results indicate that structural changes have occurred in the after doping.

Figure 3 shows the Raman spectra of different samples at 300 K. In our BFO samples, the first four strong peaks at 146.00, 175.25, 213.25, and 435.25 cm^{-1} manifest the A_1-1, A_1-2, A_1-3, and A_1-4 modes, and the remaining six small peaks at 283.25, 333.50, 370.00, 472.50, 558.50, and 611.25 cm^{-1} are assigned to the E-2, E-3, E-4, E-5, E-6, and E-7 modes, respectively. **Table 1** lists the values found in the literature and in this study for the BFO samples. The difference in the peak positions observed by different researchers may be caused by different preparation methods.

As the doping ratio increases, we can see that the peak position of the A_1-1 mode gradually shifts towards the blue and the relative peak intensity gradually decreases. It is considered that the 472.5 cm^{-1} mode in the BFO Raman spectrum corresponds to the bending vibration mode of the Fe–O bond, and the 558.5 cm^{-1} mode corresponds to the stretching vibration mode of the Fe–O bond. The peak intensity of the 472.5 cm^{-1} mode is gradually increased after the incorporation of Nd^{3+} and Co^{2+}, indicating that the bond angle of the Fe–O bond changes after the impurity is incorporated. The A_1-1 mode of the $Bi_{0.95}Nd_{0.05}Fe_{0.80}Co_{0.20}O_3$ (BNFCO-20) sample disappeared, while a new Raman mode appeared at 677.75 cm^{-1}. This apparent difference indicates a structural phase change in the
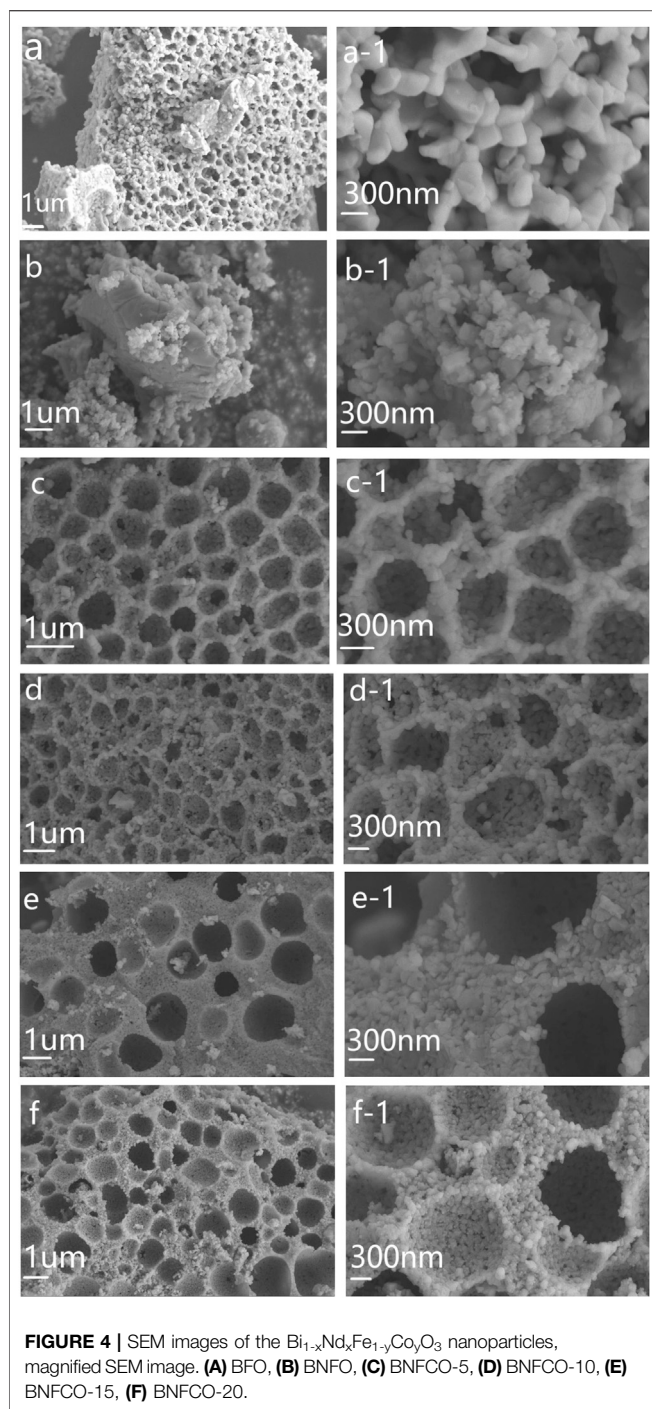
sample. The structural phase transition destroys the helical spin structure, which enhances the magnetic properties of the sample. The residual magnetization of the BNFCO-20 sample measured in this experiment is 0.68 emu g^{-1} higher than that of the undoped BFO sample.

Figure 4 shows the surface morphological features of the $Bi_{1-x}Nd_xFe_{1-y}Co_yO_3$ nanoparticles by using scanning electron microscopy (SEM). As can be seen, the prepared samples are stacked together to form a regular honeycomb shape. This did not occur in previous experiments. When Nd^{3+} and Co^{2+} are incorporated, the size of the $Bi_{1-x}Nd_xFe_{1-y}Co_yO_3$ nanoparticles gradually becomes smaller, which is in good agreement with the XRD results. The decrease in grain size destroys the cycloidal spin period (62 nm) of the BFO structure, which is consistent with the trend of the magnetic properties of the samples. This agglomeration of the nanoparticles may affect their photocatalytic properties.

Figure 5 shows UV–Visible spectra of the $Bi_{1-x}Nd_xFe_{1-y}Co_yO_3$ nanoparticles. Compared with pure BFO, the absorption spectra of all doped samples shown a clear red shift. In this paper, the band gap of all samples is calculated by using **Eq. 1**.

$$E_g = h\nu = h\nu/\lambda = 1240/\lambda \qquad (1)$$

As shown in **Table 1**, the band gap energy of BFO is greatly reduced when Nd^{3+} and Co^{3+} are incorporated. The band gap energy of the un-doped BFO sample was 2.063 eV, which is in

FIGURE 4 | SEM images of the $Bi_{1-x}Nd_xFe_{1-y}Co_yO_3$ nanoparticles, magnified SEM image. **(A)** BFO, **(B)** BNFO, **(C)** BNFCO-5, **(D)** BNFCO-10, **(E)** BNFCO-15, **(F)** BNFCO-20.

good agreement with the previously reported values. The reason for the reduction in the band gap of all $Bi_{1-x}Nd_xFe_{1-y}Co_yO_3$ nanoparticles samples may be due to the Fe-O octahedral distortion of the molecular orbitals (Sati et al. 2014). The incorporation of metal ions produces a degeneracy of the impurity level, causing the acceptor level or the donor level to move to reduce the forbidden band width (Chen et al. 2010). The results show that the presence of Nd^{3+} and Co^{2+} can reduce the band gap of BFO and make it better to absorbing visible light.

The photocatalytic activity of pure and co-doped BFO nanoparticles was studied by the degradation of 30 mg of the powder samples dissolved in 50 ml deionized water along with the addition of 0.01 g/L methylene orange (MO). The degradation of MO with the BFO nanoparticles in the dark condition for 15 h is similar to that of the blank test, which demonstrates that the absorption of RhB on the BFO is limited after the adsorption-desorption equilibrium was reached. From **Figure 5B**, we can see that the value of methylene orange (MO) peak is not decreased gradually but increased, which is special and interesting for normal photocatalytic degradation . The only possible reason is that the water is splitted and reduced under the illuminating of ultraviolet visible light, which lead to the increase of intensity of methylene orange. However, another possible reason must excluded is that the water might be evaporated under the illuminating of ultraviolet visible light. Consequently, the reaction of photocatalytic degradation without the catalyst under the same condition is conducted, which is prepared to quantitate the evaporative capacity of water during the whole reaction. The results are showed in the **Figure 5C**. Compared with these two group data as showed in **Figures 5B,C** we could draw a conclusion that the evaporation of water indeed take place during the illuminating of ultraviolet visible light, but the splitting of water without any external field bias and unassisted overall water splitting indeed occurs. The decrease is 4.5% for the blank group but the increase reaches the 7.1%. In order to further prove the splitting of water, the online detection of production of hydrogen were conducted under the protection of N_2 atmosphere. As showed in **Figure 5D**, the amount of hydrogen production of $Bi_{0.95}Nd_{0.05}Fe_{0.85}Co_{0.15}O_3$ reached 8.88umol/g after 1.5 h, however the other samples could not be detected the production of hydrogen. In order to easily understand the strength for production of hydrogen gas using doped BFO, a comparative result in form of table is shown in **Table 3**.

On the basis of above results, a tentative schematic illustration of the energy band diagram of the Nd and Co co-doped BFO photocatalyst is depicted in **Figure 6**, to explain how the photo-generated electrons in surface contribute to the hydrogen production. As we know the possible reason of unassisted water splitting with BFO is that the valence band edge and the conduction band edge of BFO straddle the water redox potentials. At the same time, the valence band edge and the conduction band edge should bend in favor of the separation of the excited electrons and holes. Firstly the band gap of $Bi_{0.95}Nd_{0.05}Fe_{0.85}Co_{0.15}O_3$ is 1.78 eV and the potential of water is 1.23 eV, which the valence band edge and the conduction band edge of BFO just straddle the water redox potentials. There are report that the optimum band gap of BFO for hydrogen production is 1.77 eV (Vishwakarma et al. 2017). A suitable band gap size is beneficial and necessary. The transfer of mobile charge carriers between the semiconductor and the contact phase produces a space-charge layer. **Figure 6** illustrates the space-charge layers produced from the mobility of charge across a semiconductor solution interface (Linsebigler et al. 1995) . The space-charge layer formed is a depletion layer,
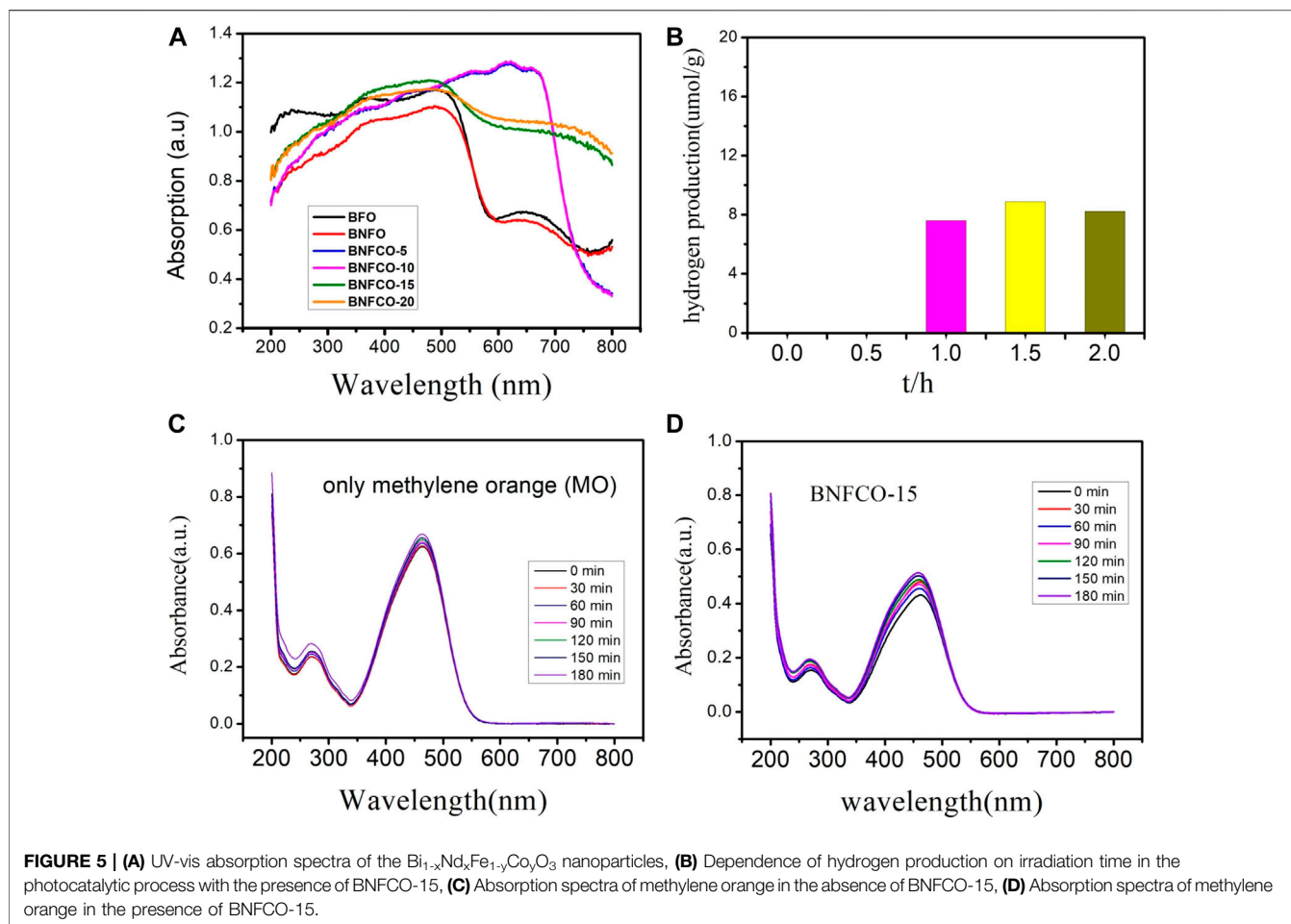
FIGURE 5 | (A) UV-vis absorption spectra of the $Bi_{1-x}Nd_xFe_{1-y}Co_yO_3$ nanoparticles, **(B)** Dependence of hydrogen production on irradiation time in the photocatalytic process with the presence of BNFCO-15, **(C)** Absorption spectra of methylene orange in the absence of BNFCO-15, **(D)** Absorption spectra of methylene orange in the presence of BNFCO-15.

TABLE 3 | Recent reports on the photocatalytic hydrogen production.

Photocatalysts	Cocatalysts	Activity		Test condition	References
		H_2(hydrogen)	O_2(oxygen)		
Bi_4NbO_8Cl	Pt	0.1 μmol/h/g	none	Methanol-water	Fang and Shangguan (2019)
$Cr-BiNb(Ta)O_4$	Pt	7 μmol/h/g	none	30% isopropanol	Fang and Shangguan (2019)
$BiPO_4$/RGO	None	30.6 μmol/h/g	none	Ethanol solution	Fang and Shangguan (2019)
$Bi_2Ti_2O_7$	None	285 μmol/h/g	none	Methanol-water	Fang and Shangguan (2019)
Bi doped $NaTaO_3$	Pt	0.86 μmol/h/g	none	Methanol-water	Fang and Shangguan (2019)
MOF	Pt	339 μmol/h/g	none	10% of lactic acid	Reddy et al. (2019)
CdS	Pt	190 μmol/h/g	none	10% of lactic acid	Shen et al. (2015)
$Gd-BiFeO_3$	Pt	60 $μmol/cm^2$	none	Na_2SO_4 aqueous solution	Yang et al. (2018)
Quantum $BiVO_4$	None	0.22 μmol/h	none	Pure water	Fang and Shangguan (2019)
Nd Co-$BiFeO_3$	None	7.8 μmol/h/g	none	Pure water	This work

TABLE 4 | Band-Gap of the $Bi_{1-x}Nd_xFe_{1-y}Co_yO_3$ nanoparticles.

Samples	BFO	BNFO	BNFCO-5	BNFCO-10	BNFCO-15	BNFCO-20
Wavelength (nm)	601	611	752	755	695	787
E (eV)	2.063	2.029	1.649	1.642	1.784	1.575

TABLE 5 | M_r and M_s value of samples at different doping ratios.

Samples	BFO	BNFO	BNFCO-5	BNFCO-10	BNFCO-15	BNFCO-20
Mr (emu/g)	0	0.012	0.273	0.493	0.555	0.679
Ms (emu/g)	0.107	0.168	0.676	1.103	1.387	1.697

FIGURE 6 | (A) Schematic depiction of the dynamic behaviors of charge carriers upon photoexcitation. **(B)** Energy band diagram of BNFCO-15 for water splitting. The band bending at the surface is caused by the space-charge region of depletion or accumulation layer.
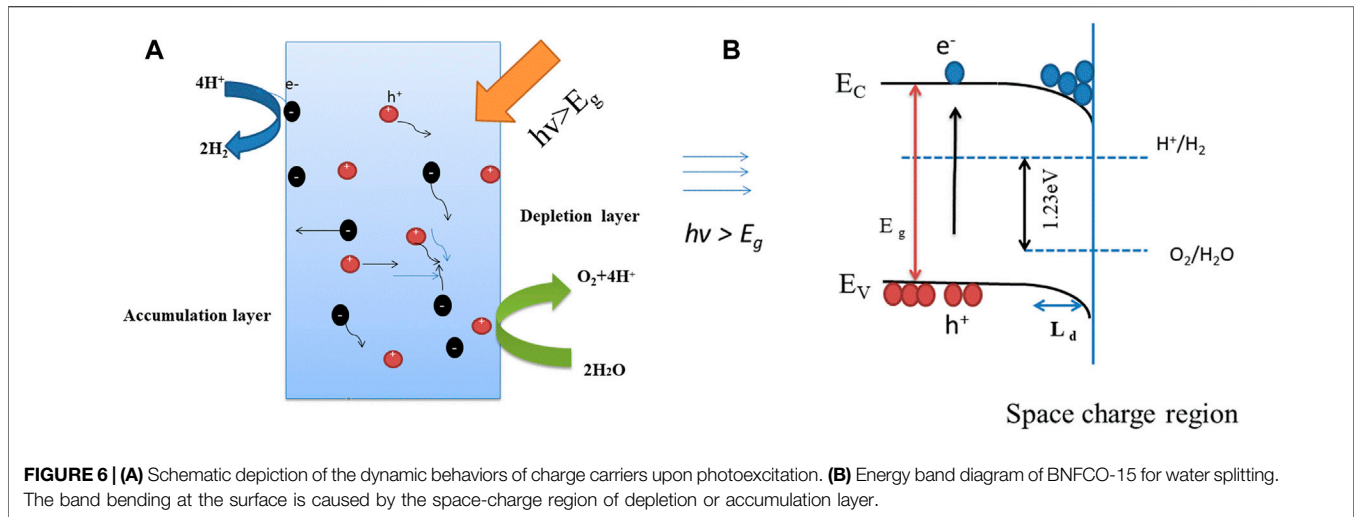
and the bands bend upward toward the surface. Because of the positive charges existence on the interface, the accumulation layer is formed and the bands would bend down in the interface. Bands with curved interfaces are stuck at either end of the water band gap like pommel horses. Because BFO is semiconductor material, when semiconductor BFO absorbs ultraviolet-light energy, electrons are excited to the conduction band (CB), while holes are present in the valence band (VB). The band curvature of the interface prevents the recombination of electrons and holes. The electrons present in the CB with protons to generate hydrogen, and the holes combine with reductive reactants to create oxidative products (Shen et al. 2015; Reddy et al. 2019). To sum up, the possible reason for this is that the conduction and valence band edges of BiFeO3 straddle the water redox potential. Consequently, it is possible to realize unassisted water splitting using BFO.

Whether the bands are bent in depletion or in accumulation, the width of the space-charge region is proportional to the Debye length (Guo et al. 2010; Fang and Shangguan, 2019) L_D.

$$L_D = \left(\frac{\varepsilon_0 \, \varepsilon_r kT}{e^2 N_D} \right)^{\frac{1}{2}} \qquad (2)$$

Where ε_0 is the permittivity of free space, ε_r is the dielectric constant of the material, and N_D is the donor density. According to **Eq. 2**, we can see that an increase in the dielectric constant can increase the Debye length and, therefore, the width of the space-charge region (Guo et al. 2010).

The magnetic hysteresis (M-H) loops of the samples at room temperature are shown in **Figure 6**. It was found that doping Nd^{3+} and Co^{2+} had a significant effect on the ferromagnetic properties of BFO nanoparticles. It can be seen from **Figure 7A** that the magnetic hysteresis loop of the un-doped BFO is almost a straight line. This phenomenon proves that the prepared BFO sample does not contain other impurity phases. As shown in **Figure 6**, as the amount of Co^{2+} doping increases, the magnetic hysteresis loop of the sample becomes more and more obvious,

and the residual magnetization and saturation magnetization gradually increase. The magnetization can be increased by increasing the doping amount of Co^{2+}, which may be mainly caused by the following two aspects. First, as the doping amount increases, the crystal structure gradually changes and the *Pnma* phase begin to appear in the parent *R3c* phase. The content of *R3c* and *Pnma* is 77.73 and 22.27% respectively in the sample $Bi_{0.95}Nd_{0.05}Fe_{0.85}Co_{0.15}O_3$. These results came from the Rietveld refinement (not shown). These changes cause the spin coupling of the cycloid to be gradually broken and increase the magnetization. Second, as the incorporation of Co increases, the cycloid spin cycle with a grain size smaller than that of the BFO structure destroys its periodicity, resulting in an increase in magnetization (Reddy et al. 2018). It is found from **Figure 7B** that an exchange bias effect occurs after the incorporation of 5% of Nd^{3+}, that is, the M-H ring undergoes an asymmetric movement along the H axis. The exchange bias effect is due to the coexistence of anisotropic FM and AFM domains (Wu et al. 2018). These results suggested that the magnetic properties of BFO nanoparticles can be enhanced by Co^{2+} and Nd^{3+} doping, which means that the photocatalyst can be separated easily by applying an external magnetic field.

Cellular architecture of Nd and Co co-doped in BFO nanoparticles, fabricated by two-solvent sol-gel method, are demonstrated as spectral photocatalytic that perform unassisted high efficiency directly produce hydrogen through splitting the water due to the optimum band-gap engineering of BFO nanoparticles was controlled by co-doping of Nd and Co. So the new material that could directly produce hydrogen through splitting the water only under the illuminating without any sacrificial agent without external bias field is urgent. Hence, Cellular architecture of Nd and Co co-doped in BFO nanoparticles, fabricated by two-solvent sol-gel method, are demonstrated as spectral photocatalytic that perform unassisted high efficiency directly produce hydrogen through splitting the water due to the optimum band-gap engineering of BFO nanoparticles was controlled by co-doping of Nd and Co.
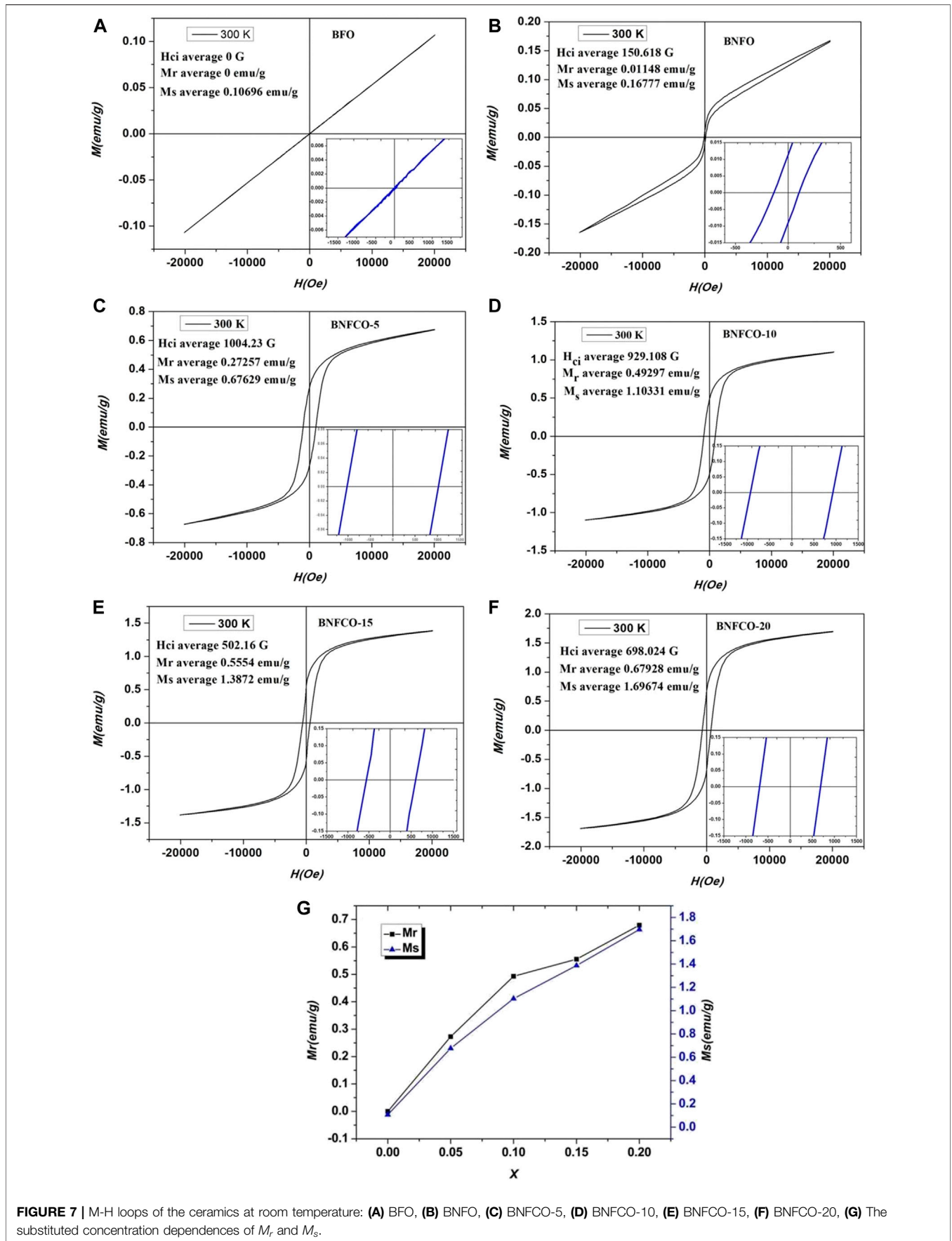
FIGURE 7 | M-H loops of the ceramics at room temperature: **(A)** BFO, **(B)** BNFO, **(C)** BNFCO-5, **(D)** BNFCO-10, **(E)** BNFCO-15, **(F)** BNFCO-20, **(G)** The substituted concentration dependences of M_r and M_s.

DATA AVAILABILITY STATEMENT

The raw data supporting the conclusions of this article will be made available by the authors, without undue reservation.

AUTHOR CONTRIBUTIONS

All authors listed have made a substantial, direct, and intellectual contribution to the work and approved it for publication

FUNDING

REFERENCES

Chen, X., Shen, S., Guo, L., and Mao, S. S. (2010). Semiconductor-based photocatalytic hydrogen generation. *Chem. Rev.* 110 (11), 6503–6570. doi:10.1021/cr1001645

Cheng, X., Shen, H., Dong, W., Zheng, F., Fang, L., Su, X., et al. (2016). Nano-Au and ferroelectric polarization mediated Si/ITO/BiFeO₃Tandem photocathode for efficient H₂ production. *Adv. Mater. Inter.* 3 (19), 1600485. doi:10.1002/admi.201600485

Chowdhury, F. A., Trudeau, M. L., Guo, H., and Mi, Z. (2018). A photochemical diode artificial photosynthesis system for unassisted high efficiency overall pure water splitting. *Nat. Commun.* 9 (1), 1707. doi:10.1038/s41467-018-04067-1

Das, K., Sarkar, B., Ghosh, S., De, S., Sinha, G., and Lahtinen, J. (2012). Enhanced magnetic and dielectric properties of Eu and Co co-doped BiFeO₃ nanoparticles. *Appl. Phys. Lett.* 101 (4), 42401. doi:10.1063/1.4738992

Dutta, D. P., Jayakumar, O. D., Tyagi, A. K., Girija, K. G., Pillai, C. G. S., and Sharma, G. (2010). Effect of doping on the morphology and multiferroic properties of BiFeO3 nanorods. *Nanoscale* 2 (7), 1149. doi:10.1039/c0nr00100g

Fang, W., and Shangguan, W. (2019). A review on bismuth-based composite oxides for photocatalytic hydrogen generation. *Int. J. Hydrog. Energ.* 44 (2), 895–912. doi:10.1016/j.ijhydene.2018.11.063

Fatima, S., Ali, S. I., Iqbal, M. Z., and Rizwan, S. (2020). Congo red dye degradation by graphene nanoplatelets/doped bismuth ferrite nanoparticle hybrid catalysts under dark and light conditions. *Catalysts* 10 (4), 367. doi:10.3390/catal10040367

Fatima, S., Irfan Ali, S., Younas, D., Islam, A., Akinwande, D., and Rizwan, S. (2019). Graphene nanohybrids for enhanced catalytic activity and large surface area. *MRS Commun.* 9 (1), 27–36. doi:10.1557/mrc.2018.194

Fukumura, H., Harima, H., Kisoda, K., Tamada, M., Noguchi, Y., and Miyayama, M. (2007). Raman scattering study of multiferroic BiFeO3 single crystal. *J. Magn. Magn. Mater.* 310 (2), e367–e369. doi:10.1016/j.jmmm.2006.10.282

Guo, R., Fang, L., Dong, W., Zheng, F., and Shen, M. (2010). Enhanced photocatalytic activity and ferromagnetism in Gd doped BiFeO3 nanoparticles. *J. Phys. Chem. C* 114 (49), 21390–21396. doi:10.1021/jp104660a

Iqbal, M. A., Tariq, A., Zaheer, A., Gul, S., and Rizwan, S. (2019a). Ti₃C₂-MXene/Bismuth ferrite nanohybrids for efficient degradation of organic dyes and colorless pollutants. *ACS Omega* 4 (24), 20530–20539. doi:10.1021/acsomega.9b02359

Iqbal, M., Fatheema, J., Noor, Q., and Rani, M. (2019b). Co-existence of magnetic phases in two-dimensional MXene. *Mater.Today. Chem.* 16, 100271. doi:10.1016/j.mtchem.2020.100271

Kothari, D., Reddy, V. R., Sathe, V., Gupta, A., Banerjee, A., and Awasthi, A. (2008). Raman scattering study of polycrystalline magnetoelectric BiFeO₃. *J. Magn. Magn. Mater.* 320 (3-4), 548–552. doi:10.1016/j.jmmm.2007.07.016

Layek, S., Saha, S., and Verma, H. C. (2013). Preparation, structural and magnetic studies on BiFe₁₋ₓCrₓO₃ (x= 0.0, 0.05 and 0.1) multiferroic nanoparticles. *AIP. Adv.* 3 (3), 032140. doi:10.1063/1.4799063

Li, S., Lin, Y.-H., Zhang, B.-P., Wang, Y., and Nan, C.-W. (2010). Controlled fabrication of BiFeO₃ uniform microcrystals and their magnetic and photocatalytic behaviors. *J. Phys. Chem. C.* 114 (7), 2903–2908. doi:10.1021/jp910401u

Linsebigler, A. L., Lu, G., and Yates, J. T., Jr (1995). Photocatalysis on TiO2 surfaces: principles, mechanisms, and selected results. *Chem. Rev.* 95 (3), 735–758. doi:10.1021/cr00035a013

Lü, F. C., Yin, K., Fu, K. X., Wang, Y. N., Ren, J., and Xie, Q. (2017). Enhanced magnetic and dielectric properties of Y doped bismuth ferrite nanofiber. *Ceram. Int.* 43 (18), 16101–16106. doi:10.1016/j.ceramint.2017.08.171

Luo, J., and Maggard, P. A. (2006). Hydrothermal synthesis and photocatalytic activities of SrTiO3-coated Fe2O3 and BiFeO3. *Adv. Mater.* 18 (4), 514–517. doi:10.1002/adma.200500109

Puhan, A., Bhushan, B., Kumar, V., Panda, H. S., Priyam, A., Das, D., et al. (2019). Tailoring the structural, optical and magnetic properties of BiFeO₃ multiferroic nanoparticles by Ba, Cr co-doping. *Mater. Sci. Eng.* 241, 48–54. doi:10.1016/j.mseb.2019.02.009

Reddy, B. P., Sekhar, M. C., Prakash, B. P., Suh, Y., and Park, S. H. (2018). Photocatalytic, magnetic, and electrochemical properties of La doped BiFeO₃ nanoparticles. *Ceram. Int.* 44 (16), 19512–19521. doi:10.1016/j.ceramint.2018.07.191

Reddy, C. V., Reddy, K. R., Harish, V. V. N., Shim, J., Shankar, M. V., Shetti, N. P., et al. (2019). Metal-Organic Frameworks (MOFs)-based efficient heterogeneous photocatalysts: synthesis, properties and its applications in photocatalytic hydrogen generation, CO₂ reduction and photodegradation of organic dyes. *Int. J. Hydrog. Energ.* 45 (13), 7656–7679. doi:10.1016/j.ijhydene.2019.02.144

Sati, P. C., Arora, M., Chauhan, S., Kumar, M., and Chhoker, S. (2014). Effect of Dy substitution on structural, magnetic and optical properties of BiFeO₃ ceramics. *J. Phys. Chem. Sol.* 75 (1), 105–108. doi:10.1016/j.jpcs.2013.09.003

Shen, L., Luo, M., Liu, Y., Liang, R., and Wu, L. (2015). Noble-metal-free MoS₂ co-catalyst decorated UiO-66/CdS hybrids for efficient photocatalytic H₂ production. *App. Catal. B.* 166-167, 445–453. doi:10.1016/j.apcatb.2014.11.056

Singh, M., Jang, H., Jo, M., and Ryu, S. (2006). Polarized Raman scattering of multiferroic BiFeO₃ epitaxial films with rhombohedral R3c symmetry. *Appl. Phys. Lett.* 88 (4), 42907. doi:10.1063/1.2168038

Vishwakarma, A. K., Tripathi, P., Srivastava, A., Sinha, A. S. K., and Srivastava, O. N. (2017). Band gap engineering of Gd and Co doped BiFeO3 and their application in hydrogen production through photoelectrochemical route. *Int. J.Hydrog. Energ.* 42 (36), 22677–22686. doi:10.1016/j.ijhydene.2017.07.153

Wang, Y., Guo, Z., Jia, Q., Dong, J., Zhang, J., and Chen, D. (2019). Effect of Nd/Mn substitution on the structure and magnetic properties of nano-BiFeO3. *J. Alloy. Compd.* 786, 385–393. doi:10.1016/j.jallcom.2019.01.369

Wu, H., Xue, P., Lu, Y., and Zhu, X. (2018). Microstructural, optical and magnetic characterizations of BiFeO₃ multiferroic nanoparticles synthesized via a sol-gel process. *J. Alloy. Compd.* 731, 471–477. doi:10.1016/j.jallcom.2017.10.087

Yang, Y., Kang, L., and Li, H. (2018). Enhancement of photocatalytic hydrogen production of BiFeO₃ by Gd³⁺ doping. *Ceram. Int.* 45 (6), 8017–8022. doi:10.1016/j.ceramint.2018.12.150

Yang, Y., Sun, J. Y., Zhu, K., Liu, Y. L., Chen, J., and Xing, X. R. (2009). Raman study of BiFeO3 with different excitation wavelengths. *Phys. B.* 404 (1), 171–174. doi:10.1016/j.physb.2008.10.029

Yuan, G. L., Liu, J. M., and Liu, Z. G. (2006). Structural transformation and ferroelectromagnetic behavior in single-phase Bi₁₋ₓNdₓFeO₃ multiferroic ceramics. *Appl. Phys. Lett.* 89 (5), 052905. doi:10.1063/1.2266992

Yuan, G. L., Or, S. W., and Chan, H. L. W. (2007). Raman scattering spectra and ferroelectric properties of Bi1−xNdxFeO3 (x=0-0.2) multiferroic ceramics. *J. Appl. Phys.* 101 (6), 064101. doi:10.1063/1.2433709